Comparative analysis of the MyTH4-FERM myosins reveals insights into the determinants of actin track selection in polarized epithelia

Samaneh Matoo†, Maura J. Graves†, Prashun Acharya, Myoung Soo Choi, Zachary A. Storad, Rawnag A. El Sheikh Idris, Brooke K. Pickles, Taylen O. Arvay, Paula E. Shinder, Andrew Gerts, Jacob P. Papish, and Scott W. Crawley*
Department of Biological Sciences, University of Toledo, Toledo, OH 43606

ABSTRACT **MyTH4-FERM (MF) myosins evolved to play a role in the creation and function of a variety of actin-based membrane protrusions that extend from cells. Here we performed an analysis of the MF myosins, Myo7A, Myo7B, and Myo10, to gain insight into how they select for their preferred actin networks. Using enterocytes that create spatially separated actin tracks in the form of apical microvilli and basal filopodia, we show that actin track selection is principally guided by the mode of oligomerization of the myosin along with the identity of the motor domain, with little influence from the specific composition of the lever arm. Chimeric variants of Myo7A and Myo7B fused to a leucine zipper parallel dimerization sequence in place of their native tails both selected apical microvilli as their tracks, while a truncated Myo10 used its native antiparallel coiled-coil to traffic to the tips of filopodia. Swapping lever arms between the Class 7 and 10 myosins did not change actin track preference. Surprisingly, fusing the motor-neck region of Myo10 to a leucine zipper or oligomerization sequences derived from the Myo7A and Myo7B cargo proteins USH1G and ANKS4B, respectively, re-encoded the actin track usage of Myo10 to apical microvilli with significant efficiency.**

Monitoring Editor
Alpha Yap
University of Queensland

Received: Jul 27, 2020
Revised: Aug 17, 2021
Accepted: Aug 26, 2021

INTRODUCTION

Myosins are a superfamily of actin-based motors that participate in numerous cellular processes such as cell motility, control of membrane protrusions and cellular shape, and the intracellular transport of cargo molecules (Heissler and Sellers, 2016). The defining feature of this superfamily is a conserved N-terminal motor domain that binds actin and hydrolyzes ATP to convert chemical energy to mechanical force. Following the motor domain is a short neck region that contains a variable number of "IQ" motifs that associate with light chains that stabilize the neck, allowing the neck to act as a rigid lever arm during force production (Uyeda *et al.*, 1996). In some myosins, the lever arm is extended using sequences that fold into a stable single α-helix (SAH) (Baboolal *et al.*, 2009). Finally, myosins contain a C-terminal tail region which is the most diverse sequence found across the superfamily. One group of interest are the myosins that contain coupled MyTH4-FERM (myosin tail homology–band 4.1, ezrin, radixin, moesin; MF) domains in their tails. A MF tandem domain is comprised of an N-terminal helical MyTH4 domain and a C-terminal clover leaf-shaped FERM domain, with the latter typically playing the dominant role in associating with binding partners (Planelles-Herrero *et al.*, 2016; Li *et al.*, 2017b). Vertebrate myosins that possess MF domains include the Class 7, 10, and 15 myosins. These myosins are proposed to use their tails to function, at least in part, as cargo transporters along actin tracks associated with membrane protrusions that extend from cells (Weck *et al.*, 2017; Houdusse and Titus, 2021).

A prevailing theory in the field is that MF myosins must dimerize in order to bring together two motor domains to allow them to "walk" on actin in a processive manner (Siththanandan and Sellers,

This article was published online ahead of print in MBoC in Press (http://www.molbiolcell.org/cgi/doi/10.1091/mbc.E20-07-0494) on September 2, 2021.

Conflict of interest: The authors declare that they have no conflicts of interest with the contents of this article.

†These authors contributed equally to this study.

*Address correspondence to: Scott W. Crawley (william.crawley@utoledo.edu).

Abbreviations used: BB, brush border; FBS, fetal bovine serum; IMAC, intermicrovillar adhesion complex; KD, knockdown; LK, linker segment; MF, MyTH4-FERM; PBS, phosphate-buffered saline; SAH, single α-helix.

2011). This is well studied for Myo10 which plays a critical role in the formation and extension of filopodia, dynamic protrusions that cells use to probe their environment. Myo10 contains a neck region comprised of three IQ motifs and a SAH motif, followed by a coiled-coil sequence that mediates antiparallel dimerization to promote a processive form of the myosin (Lu *et al.*, 2012). Importantly, the C-terminal cargo-binding tail of Myo10 is dispensable for its ability to track to filopodia tips (Tokuo *et al.*, 2007). Detailed studies have begun to produce a model of how Myo10 traffics on the parallel-bundled actin of filopodia. Antiparallel dimerization and an unusually large powerstroke swing angle (~120°) promote a geometry of the lever arms that place the two motor domains of the Myo10 dimer relatively far apart during stepping. The innate length of the Myo10 lever arm is ~24 nm, allowing the myosin to achieve steps of ~52, 40, and possibly 57 nm when in an antiparallel dimer (Ropars *et al.*, 2016). Large step sizes between 47 and 57 nm are not easily achieved on single actin filaments due to the actin filament twist that places myosin binding sites on opposite faces of the actin filament between these distances. Rather, stepping of Myo10 is proposed to be compatible with the bundled actin found in filopodia, in which myosin binding sites on neighboring filaments are located at distances of 52, 57, 38, and 19 nm. This suggests the geometry of Myo10 favors walking on the surface of bundled actin in which the myosin dimer straddles two adjacent filaments to accommodate its large step size (Nagy *et al.*, 2008; Ropars *et al.*, 2016).

In contrast to Myo10, much less is known about the stepping mechanics of the two Class 7 MF myosins found in vertebrates, Myo7A and Myo7B (Bement *et al.*, 1994; Chen *et al.*, 1996, 2001). Myo7A has been largely characterized as part of the Usher syndrome adhesion complex associated with stereocilia of the inner ear that mediates sound reception (Weil *et al.*, 1995, 1996). Myo7B functions in a homologous manner as part of the intermicrovillar adhesion complex (IMAC) found at the distal tips of brush border (BB) microvilli on the surface of the solute-transporting epithelia of the intestine and kidney (Crawley *et al.*, 2014b, 2016; Weck *et al.*, 2016; Choi *et al.*, 2020). Myo7A and Myo7B each possess five homologous IQ motifs in their lever arm, while the post-IQ region of Myo7A also contains a SAH motif. Their five IQ motifs would span a theoretical length of ~19 nm when stabilized by light chains, with the SAH motif of Myo7A further extending the lever arm an additional ~9 nm (Li *et al.*, 2017a). The powerstroke swing angles of these myosins have not been measured to date. Both of these myosins have a tail comprised of a pair of MF domains separated by an intervening SH3 domain, but lack an intrinsic dimerization sequence and are thought to be monomeric on their own (Chen *et al.*, 2001; Umeki *et al.*, 2009; Yang *et al.*, 2009). Binding of oligomeric cargo to their tail sequences is one mechanism proposed to promote their processive forms. Previous groups have successfully used forced dimerization systems (e.g., variants of leucine zippers and the FK506 binding protein inducible dimerization domain) to study the properties of both Myo7A and Myo7B in the absence of cargo (Yang *et al.*, 2006; Sakai *et al.*, 2011, 2015; Weck *et al.*, 2016; Sato *et al.*, 2017). The nature of oligomerization imparted from IMAC or Usher complex cargo molecules, and how oligomerization would influence lever arm geometry, is not presently clear for the Class 7 myosins.

MF myosins associate with a variety of membrane protrusions that have a core common feature: each protrusion is supported by a parallel-bundled array of actin filaments that have their barbed ends oriented toward the distal tip of the protrusion. However, the dimensions of the specific type of protrusion, the number of actin filaments they contain, and the actin cross-linking proteins that organize them differ partially across each protrusion type. For example, the largest stereocilia of the inner ear achieve a height of ~100 µm and are supported by hundreds of actin filaments that are cross-linked to an interfilament distance of ~10 nm by a variety of actin bundling factors including espin, fimbrin/plastin, fascin-2, XIRP2, and TRIOBP (Sekerkova *et al.*, 2006; Kitajiri *et al.*, 2010; Chou *et al.*, 2011; Francis *et al.*, 2015; Scheffer *et al.*, 2015; Taylor *et al.*, 2015). In comparison, BB microvilli range in length from 0.5 to 3 µm and contain 30–40 actin filaments that are bundled primarily by espin, fimbrin/plastin, and villin with a reported interfilament distance of ~13 nm (Bretscher and Weber, 1979, 1980; Mooseker *et al.*, 1980; Matsudaira *et al.*, 1983; Bartles *et al.*, 1998; Ohta *et al.*, 2012). Filopodia can be upward of 10 µm in length and contain 10–30 actin filaments that are bundled primarily by fascin that packs adjacent filaments ~12 nm apart (Yang *et al.*, 2013). Interestingly, these different types of actin-based protrusions can often coexist on the same cell, leading to an important series of questions: can the MF myosins differentiate between distinct parallel-bundled actin networks? If so, what are the structural features of these myosins that allow them to do so?

Here we performed a comparative analysis of Myo7A, Myo7B, and Myo10 using CACO-2_{BBE} enterocytes as a model. The advantage of this system is that CACO-2_{BBE} cells create well-developed apical microvilli that are spatially separated from basal filopodia due to the columnarlike shape the cells attain on polarization. This allows us to easily observe which of these two parallel-bundled actin networks that a particular myosin "chooses" when expressed in this cell line. We questioned whether we could influence actin track selection by modulating either the lever arm composition or the mode of oligomerization of the myosin in order to control the overall lever arm geometry. Together, our study provides novel insights into the mechanism underlying how myosins are able to select between different parallel-bundled actin networks in polarized cells.

RESULTS

Full-length Myo7A does not target to the apical domain of enterocytes

To begin to dissect how the MF myosins select for their preferred actin networks in cells, we first questioned whether Myo7A was able to utilize BB actin as a track similar to Myo7B. Myo7A and Myo7B exhibit an overall identity of ~56% (Supplemental Figure S1A) and associate with a homologous set of cargo molecules within their respective adhesion complexes (Crawley *et al.*, 2014a). Previous proteomic analysis of isolated enterocyte BBs detected low amounts of Myo7A in addition to the abundant levels of Myo7B (McConnell *et al.*, 2011). We confirmed by immunoblot analysis that Myo7A is indeed expressed in the gut alongside Myo7B (Supplemental Figure S1B). However, localization studies in mouse duodenal tissue revealed only minor levels of fluorescence signal for Myo7A within the BB (Supplemental Figure S1C), in contrast to the robust signal of Myo7B detected at microvillar tips (see the arrows in the zoom inset in Supplemental Figure S1D and the line-scan analysis in Supplemental Figure S1E). To further explore the BB-targeting capabilities of Myo7A, we expressed the full-length protein (Figure 1A; Myo7A FL) as an EGFP-fusion in CACO-2_{BBE} cells. CACO-2_{BBE} cells are a malleable enterocyte model system that utilizes the IMAC to construct a near tissuelike BB after an extended period in cell culture (Peterson and Mooseker, 1993; Crawley *et al.*, 2014b). Targeting was quantified by calculating the ratio of EGFP signal found in the BB versus the cytosol. As a control, a cell line expressing EGFP-tagged full-length Myo7B was created (Figure 1A; Myo7B FL). While Myo7B exhibited robust targeting to BB microvilli (Figure 1, B and G), Myo7A was largely cytosolic with only low amounts of the myosin

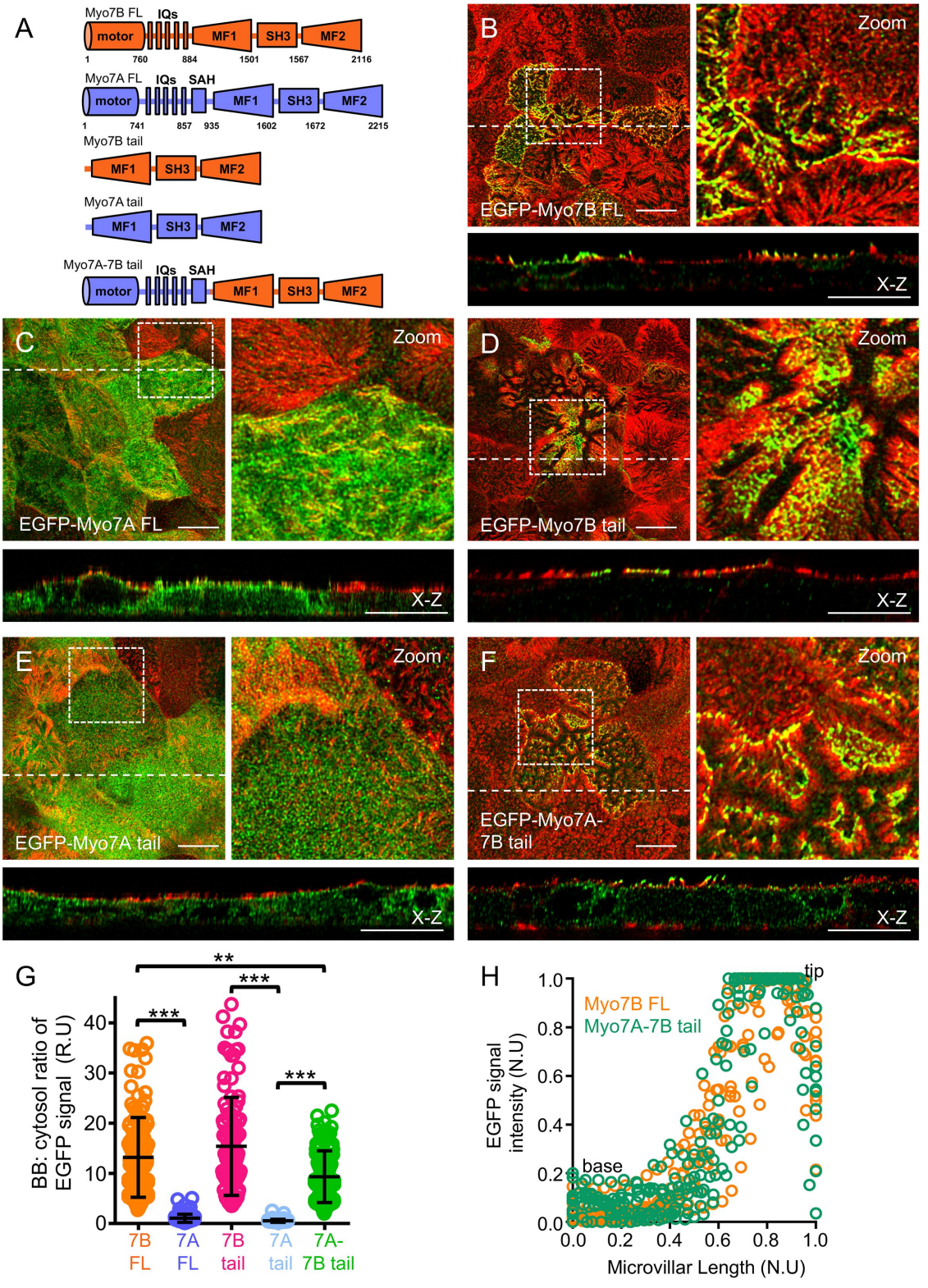

FIGURE 1: Myo7A does not target to apical microvilli in polarized CACO-2_{BBE} cells. (A) Diagram of EGFP-fusion constructs used to assess the apical targeting ability of Myo7A in CACO-2_{BBE} cells. Amino acid position numbers are shown for full-length (FL) Myo7A and Myo7B to illustrate relative size of domains. (B–F) Confocal images of 12-d polarized CACO-2_{BBE} cells stably expressing EGFP-fusion constructs tested. Dashed lines indicate the position where X-Z sections were taken; X-Z sections are shown below each en face image. Scale bars, 10 μm. (G) Scatterplot quantification of the BB:cytosol ratios of EGFP signal for all EGFP-fusion constructs tested. Bars indicate mean and SD. R.U = relative units. $^{**}p < 0.001$, $^{***}p < 0.0001$, two-tailed *t* test. (H) Line-scan analysis of EGFP-Myo7B FL (orange) and EGFP-Myo7A-7B tail chimera (green) signal intensity collected parallel to the microvillar axis in stably transduced CACO-2_{BBE} cells. Microvillar length has been normalized, where 0 = base of microvilli, and 1 = distal tip of microvilli. N.U = normalized units.

localizing to the BB (Figure 1, C and G). We next explored whether the lack of robust targeting of Myo7A was due to differences in its cargo-binding properties compared with Myo7B. It has previously been shown that the isolated tail of Myo7B can target to microvilli through interactions with endogenous IMAC cargo (Weck *et al.*, 2016). To test whether Myo7A exhibited similar properties, the tail domains of Myo7A and Myo7B were stably expressed in CACO-2_{BBE} cells (Figure 1A; Myo7A tail, Myo7B tail). Similar to the full-length proteins, the tail of Myo7B was able to target to the BB (Figure 1, D and G), while the tail of Myo7A was found in the cytosol (Figure 1, E and G). Consistent with this, swapping the tail domain of Myo7B into full-length Myo7A (Figure 1A; Myo7A-7B tail) promoted targeting of this chimera to the BB (Figure 1, F and G), where it exhibited a similar enrichment at the microvillar tips as seen with full-length Myo7B (Figure 1H).

Myo7A is thought to exist in an autoinhibited conformation in which the tail domain folds back to silence motor activity (Umeki *et al.*, 2009; Yang *et al.*, 2009). Evidence suggests that cargo binding to the tail relieves inhibition, providing a mechanism for correct temporal activation of Myo7A in cells (Sakai *et al.*, 2011; Liu *et al.*, 2021). We reasoned that the lack of targeting of full-length Myo7A could result from either its motor domain not being "compatible" with using BB actin as a track (perhaps due to differences in actin cross-linking proteins found between BB and stereocilia that could impact actin structure),or that Myo7A was not being properly activated in enterocytes due to lack of correct cargo for its tail domain. To begin to assess this, we tested whether our Myo7A-Myo7B tail chimera could rescue the BB assembly defects associated with the loss of endogenous Myo7B. Stable knockdown (KD) of Myo7B from CACO-2_{BBE} cells disrupts proper IMAC distal tip targeting and adhesion activity, leading to impaired microvillar clustering and the formation of abnormal BBs (Figure 2, A and B; Supplemental Figure S2, A and B). Successful rescue of these defects requires both a functional motor domain and the intact tail of Myo7B (Weck *et al.*, 2016). We attempted to rescue proper IMAC-mediated microvillar clustering in stable Myo7B KD cells by expressing EGFP-tagged KD-refractory versions of Myo7B FL, Myo7A FL, and our Myo7A-Myo7B tail chimera. While Myo7A FL was unable to rescue microvillar clustering, both Myo7B FL and the Myo7A-Myo7B tail chimera restored microvillar clustering to similar levels (Figure 2, A and B). In sum, these data suggest Myo7A and Myo7B are not functionally redundant in the gut, and that differences between their tail domains rather than their motor activity likely specify their proper in vivo roles.

A forced dimer of Myo7A can utilize BB actin tracks

Previous studies have employed forced dimer systems to explore the properties of the Class 7 myosins in the absence of cargo binding (Yang *et al.*, 2006; Sakai *et al.*, 2011, 2015; Weck *et al.*, 2016; Sato *et al.*, 2017). Fusing the motor-neck region of Myo7B with a GCN4 parallel dimer leucine zipper motif (Figure 3A; Myo7B-MN-GCN4) promoted targeting of the chimera to the distal tips of BB microvilli when expressed in CACO-2_{BBE} cells (Figure 3, B and G). We used an identical approach to further investigate whether the motor domain of Myo7A was able to use the actin track found in BB microvilli in the absence of any associated tail sequence. For our analysis, targeting of constructs was quantified by binning cells into one of three categories: those exhibiting no targeting, apical targeting (but not exclusively at the distal tips of microvilli), or distal tip targeting of the EGFP-fusion protein. Similar to Myo7B, a forced dimer of Myo7A (Figure 3A; Myo7A-MN-GCN4) targeted to the distal tips of microvilli (Figure 3, C and G). Incorporating a mutation (R212A) expected to block phosphate release and inhibit actin binding of Myo7A abolished apical targeting, confirming that motor activity was essential for its correct localization (Figure 3, D and G).

We used this forced dimer system to explore how differences in the lever arm between Myo7A and Myo7B impacted targeting. Both myosins have five homologous IQ motifs following their motor domains, while Myo7A has a further SAH motif that extends its neck. Deletion of the IQ motifs abolished targeting of the Myo7A forced dimer, suggesting that the SAH motif alone cannot function as an adequate lever arm and that loss of the IQ motifs may lead to impaired motor function (Figure 3, E and G). Surprisingly, shortening the lever arm of Myo7A by deleting the SAH motif (Figure 3A; Myo7A-$MN_{\Delta SAH}$-GCN4) had an intermediate effect: this deletion mutant was able to target to the BB, but did not appear exclusively restricted to the distal tips of microvilli (Figure 3, F and G). This was easily observed by comparing targeting of this construct versus wild-type forced dimers in mature microvilli that were undergoing IMAC-mediated clustering (Supplemental Figure S3, A–D). We confirmed this by measuring the signal distribution across the BB axis using line-scan analysis. While the wild-type Myo7A forced dimer displayed obvious enrichment toward the distal tips of microvilli, deleting the SAH motif resulted in signal being detected across the entire microvillar axis (Figure 3, H and I). This suggests that the Myo7A SAH motif is an integral component of its neck region and likely plays a more complex role beyond simply lengthening the lever arm compared with Myo7B. Together, these results reveal that a forced parallel dimer of Myo7A can target to the distal tips of BB microvilli, and that the longer theoretical length of the Myo7A lever arm does not preclude this myosin from associating with apical microvilli.

MF myosin lever arm identity does not define actin track usage

We next sought to directly compare two MF myosins that utilize different actin networks in cells. For this, we compared Myo7B that targets to microvillar actin tracks to Myo10 that has evolved to traffic on filopodia actin. More specifically, we first questioned whether lever arm identity could help specify which actin network a MF myosin utilizes. This could occur through the lever arm sensing local calcium levels found in distinct actin networks in order to control motor activity based on location, or perhaps due to differences in the lever arm-influenced step sizes of myosins that may be fine-tuned to match specific actin networks. Previous work has shown that the minimal processive form of Myo10 (herein referred to as "minimal Myo10") that tracks to filopodia tips requires its motor domain, neck region, and native antiparallel coiled-coil (Figure 4A; Myo10-MN-CC) (Berg and Cheney, 2002). We tested whether minimal Myo10 could target correctly to the basal region in CACO-2_{BBE} cells. To assess this, a stable cell line expressing EGFP-tagged minimal Myo10 was created and imaged at both an early confluency time point (~1 d after plating, prior to BB assembly) to visualize filopodia only (Supplemental Figure S4B) and at a 12-d postconfluency polarized time point to observe mature microvilli and basal filopodia in the same cell (Figure 4C). Minimal Myo10 was exclusively associated with the basal region of cells at both time points, exhibiting prominent targeting to filopodia protrusions that were easily identified at the early confluency stage. Importantly, minimal Myo10 did not target to apical microvilli in polarized cells, identical to previous observations examining expression of full-length Myo10 in MDCK kidney epithelial cells (Liu *et al.*, 2012). This suggests that the determinants for actin track selection utilized by Myo10 in epithelia are likely encoded in the minimal form of the myosin. The efficiency of

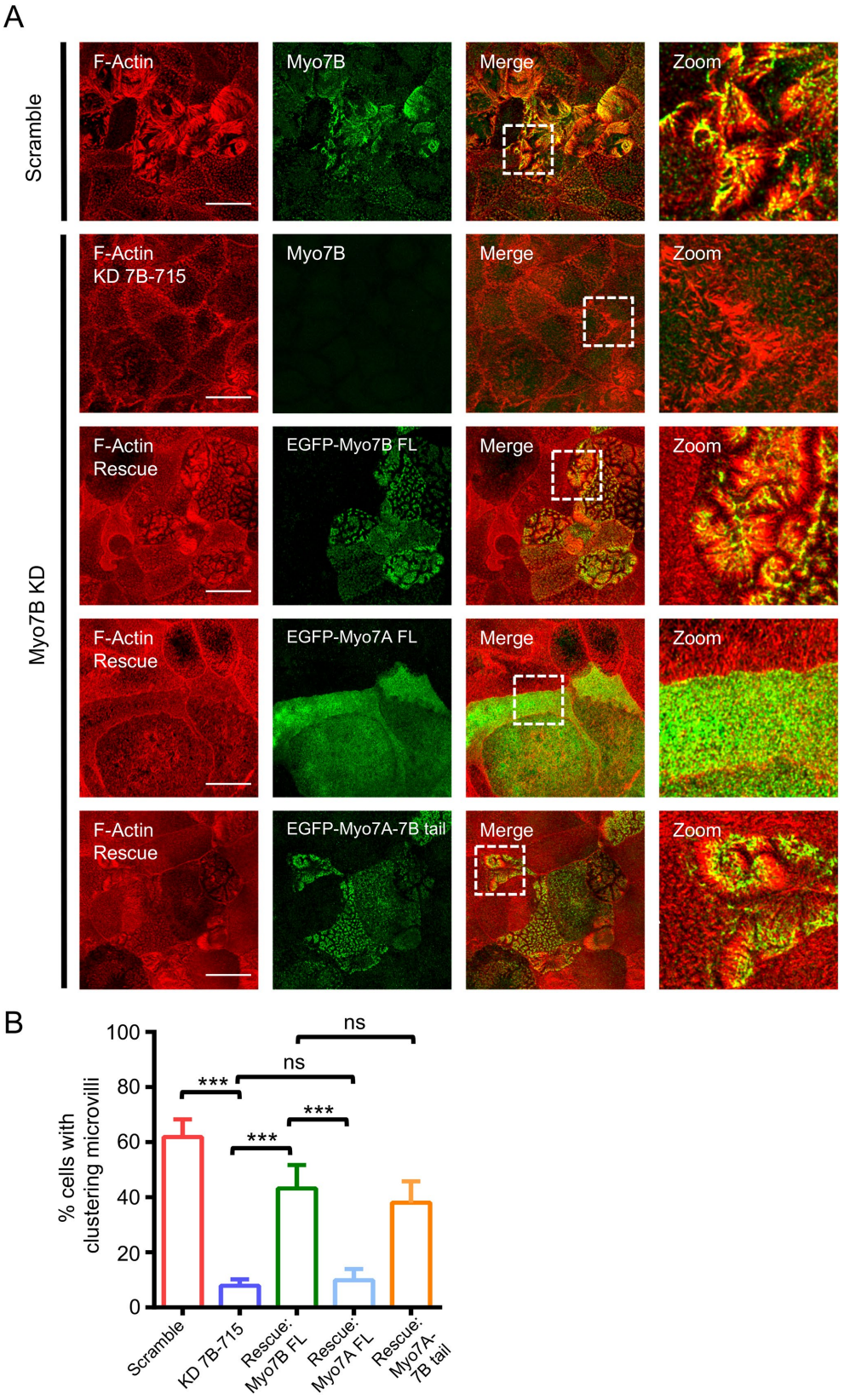

FIGURE 2: Myo7A is not functionally redundant to Myo7B in supporting IMAC-mediated BB assembly in polarized CACO-2_{BBE} cells. (A) Confocal images of 12-d polarized CACO-2_{BBE} cells stably expressing either an shRNA construct or both shRNA and an EGFP-fusion rescue construct. Cells were stained for F-actin (red) and either Myo7B (green) for scramble and KD cell lines, or EGFP (green) for rescue cell lines. Boxed regions denote areas in zoomed panels for each image set. Scale bars, 20 μm (B) Quantification of microvillar clustering in KD and rescue CACO-2_{BBE} cell lines. For quantification of rescue cell lines, only EGFP-positive cells were scored. Scramble control, $n = 384$ cells; Myo7B KD 715, $n = 345$ cells; Myo7B KD 715 rescue EGFP-Myo7B FL, $n = 156$ cells; Myo7B KD 715 rescue EGFP-Myo7A FL, $n = 187$ cells; Myo7B KD 715 rescue EGFP-Myo7A-7B tail chimera, $n = 121$; ns = not significant, $***p < 0.0001$, two-tailed *t* test. Bars indicate mean ± SD.

basal targeting was quantified by detecting the number of EGFP puncta above a set threshold value, expressed per unit of basal surface area (see *Materials and Methods* for details). This revealed that the level of basal targeting of minimal Myo10 was only slightly lower in polarized cells compared with early confluency cells (compare Figure 4B and Supplemental Figure S4A).

A variant of minimal Myo10 lacking its SAH motif was engineered to test whether shortening the lever arm would cause Myo10 to change its actin track preference (Figure 4A; Myo10-MN-ΔSAH-CC). Deletion of the Myo10 SAH motif did not result in apical targeting, but did significantly reduce basal targeting at both early confluency (Supplemental Figure S4, A and C) and polarized time points (Figure 4, B and D). We further investigated whether the specific identity of the lever arm could influence actin track selection by testing two more variants of Myo10: one in which Myo10 retained its native SAH motif but the IQ motifs of Myo7B were swapped in (Figure 4A; Myo10-MN_{7BIQs}-CC) and another in which the Myo7B IQ motifs alone served as the lever arm for Myo10 (Figure 4A; Myo10-MN_{7BIQs}-ΔSAH-CC). Minimal Myo10 containing the IQ motifs of Myo7B still exhibited striking selectivity for filopodia actin tracks and did not target to apical microvilli in polarized cells (Figure 4E). The level of targeting to the basal region for this construct was similar to wild-type minimal Myo10 at early confluency (Supplemental Figure S4, A and D), but decreased below wild-type levels in polarized cells (Figure 4, B and E). The variant of minimal Myo10 in which the Myo7B IQ motifs served as the sole lever arm (Myo10-MN_{7BIQs}-ΔSAH-CC) exhibited reduced tracking to filopodia tips at both early

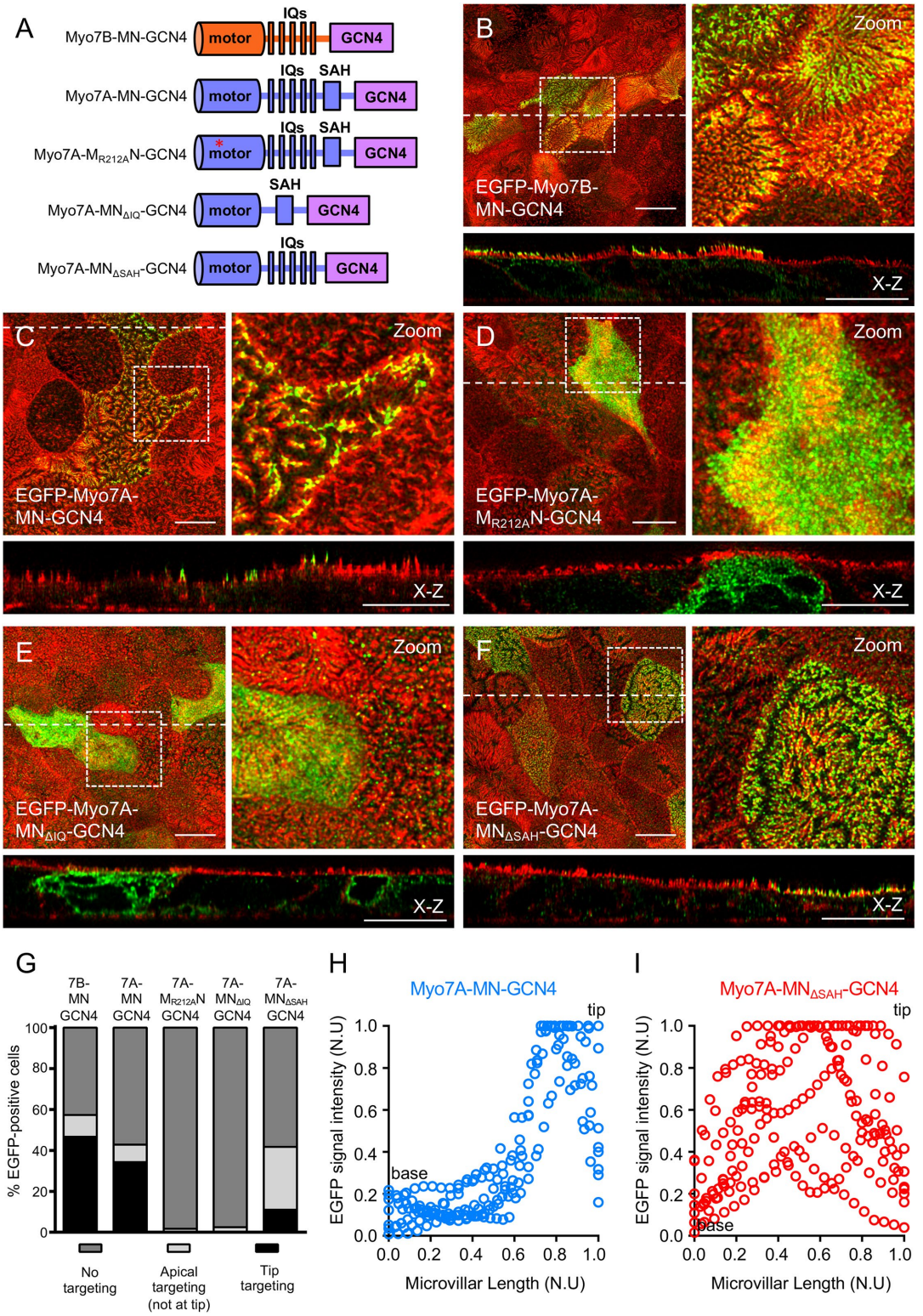

FIGURE 3: A GCN4-mediated forced dimer of Myo7A targets to the distal tips of BB microvilli in polarized CACO-2$_{BBE}$ cells. (A) Diagram of EGFP-fusion constructs used to assess the apical targeting ability of forced dimer variants of motor-neck (MN) regions of Myo7A and Myo7B. (B–F) Confocal images of 12-d polarized CACO-2$_{BBE}$ cells stably expressing EGFP-fusion constructs tested. Boxed regions denote areas in zoomed panels for each figure. Dashed lines indicate the position where X-Z sections were taken; X-Z sections are shown below each en face image. Scale bars, 20 μm. (G) Quantification of apical targeting. Myo7B-MN-GCN4, $n = 56$ cells; Myo7A-MN-GCN4, $n = 52$ cells; Myo7A-M$_{R212A}$N-GCN4, $n = 76$ cells; Myo7A-MN$_{\Delta SAH}$-GCN4, $n = 64$ cells; Myo7A-MN$_{\Delta IQ}$-GCN4, $n = 49$ cells. Stacked bars indicate mean. (H, I) Line-scan analysis of EGFP-Myo7A-MN-GCN4 (blue) and Myo7A-MN$_{\Delta SAH}$-GCN4 (red) signal intensity collected parallel to the microvillar axis. Microvillar length has been normalized, where 0 = base of microvilli and 1 = distal tip of microvilli. N.U = normalized units.

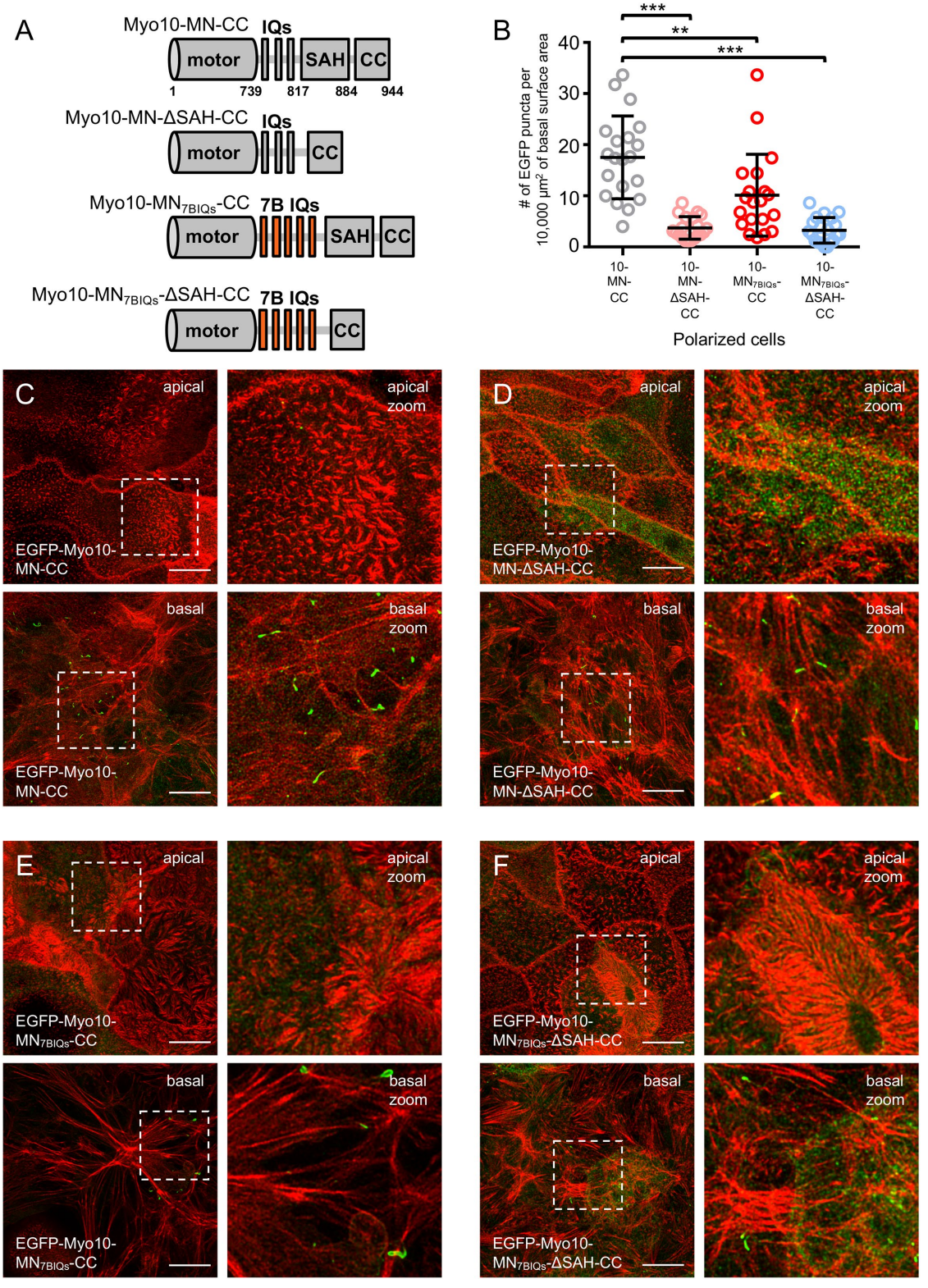

FIGURE 4: Lever arm identity does not dictate actin track selection of Myo10 expressed in polarized CACO-2_{BBE} cells. (A) Diagram of EGFP-fusion constructs that were used to assess the role of the lever arm in actin track selection of Myo10 variants expressed. Amino acid position numbers are shown for Myo10-MN-CC to illustrate relative size of domains. (B) Quantification of the number of EGFP puncta per 10,000 μm^2 of basal surface area from 12-d polarized CACO-2_{BBE} cells stably expressing EGFP-tagged variants of Myo10. See *Materials and Methods* for details. $^{**}p < 0.001$, $^{***}p < 0.0001$, two-tailed *t* test. Bars indicate mean ± SD. (C–F) Confocal images of the apical (top panels) and basal regions (bottom panels) from a representative image stack of 12-d polarized CACO-2_{BBE} cells stably expressing EGFP-fusion constructs tested. Boxed regions denote areas in zoomed panels for each figure. Scale bars, 20 μm.

confluency (Supplemental Figure S4, A and E) and polarized time points (Figure 4, B and F), but also did not target to apical microvilli.

To gain insight into whether modulating the lever arm of Myo7B could influence actin track selection, we first imaged our wild-type EGFP-tagged Myo7B forced dimer at early confluency to examine if targeting to basal filopodia occurred prior to the onset of BB assembly. This revealed diffuse localization of the Myo7B forced dimer in the cytoplasm, with no obvious localization to basal actin structures (Supplemental Figure S5A). On polarization, the Myo7B forced dimer targeted to apical microvilli while still exhibiting no localization to the basal region of cells (Figure 5, B and C). Indeed, direct side-by-side comparison of the Myo7B forced dimer to minimal Myo10 expressed in polarized cells exemplified the striking selectivity in actin track usage by these two myosins (Supplemental Figure S5, C and D). We proceeded to swap the IQ motifs and the SAH motif of Myo10 into our Myo7B forced dimer (Figure 5A; Myo7B-MN_{10neck}-GCN4) to test whether the identity of the neck region could influence actin track selection for Myo7B. This variant of Myo7B exhibited targeting to apical microvilli similar to the wild-type Myo7B forced dimer, with no apparent basal targeting at either early confluency (Supplemental Figure S5B) or after polarization (Figure 5, B and D). In sum, these results suggest that the specific identity of the lever arm does not dictate which actin network is used by the MF myosins.

Mode of oligomerization and motor domain identity influence actin track selection

While the innate length of the lever arm contributes to the distance that can be achieved between two motor domains of a dimerized myosin (Uyeda *et al.*, 1996), the mode of dimerization (parallel vs. antiparallel) plays a greater role in dictating the "reach" of a dimerized motor during stepping. To explore whether the specific mode of dimerization could influence actin track selection of the MF myosins, we tested a GCN4 leucine zipper parallel dimerization motif in place of the native antiparallel coiled-coil of Myo10. We first confirmed that deletion of the antiparallel coiled-coil motif from minimal Myo10 (Figure 6A; Myo10-MN) abolished trafficking to filopodia tips at both early confluency (Supplemental Figure S6, A–C) and polarized time points in CACO-2_{BBE} cells (Figure 6, B–D). This demonstrated that oligomerization is strictly required for targeting of Myo10 in our cell system. We utilized a similar design as previously described to create a parallel dimerized Myo10 (Caporizzo *et al.*, 2018), in which a GCN4 sequence was fused in register with its SAH motif (Figure 6A; Myo10-MN-GCN4). This form of Myo10 was shown to be active in vitro, exhibiting processive motility on both single actin filaments and fascin-bundled actin (Caporizzo *et al.*, 2018). We observed robust targeting of the parallel dimerized Myo10 to tips of basal protrusions in our CACO-2_{BBE} cells imaged at early confluency (Supplemental Figure S6, A–D). In contrast, the parallel dimerized Myo10 shifted to target predominantly to the distal tips of apical microvilli in polarized cells (Figure 6, B and E). We did observe rare examples of cells that had both apical and basal targeting at the same time, though these cells were likely immature in terms of polarization and were typically associated with areas of the monolayer that had small gaps (Supplemental Figure S6E, see the zoom panel in the basal view). Quantification revealed that the efficiency of apical targeting of the parallel dimerized Myo10 was lower compared with our Myo7B forced dimer (Figure 6, B and F).

Given that the GCN4 parallel dimerization sequence could support Myo10 targeting to both basal filopodia and apical microvilli, we questioned whether the antiparallel coiled-coil of Myo10 could be utilized by Myo7B and whether it influenced actin track selection. Surprisingly, fusing either the Myo7B motor-neck fragment to the isolated antiparallel coiled-coil of Myo10 (Figure 7A; Myo7B-MN-10 CC) or the isolated Myo7B motor domain to both the lever arm and the antiparallel coiled-coil of Myo10 (Figure 7A; Myo7B-MN_{10neck}-10 CC) failed to support targeting to apical microvilli in polarized monolayers (Figure 7, B–E) or basal filopodia in early confluency cells (Supplemental Figure S7, A and B). Indeed, we did not observe any case of targeting of Myo7B to basal filopodia irrespective of the design of the particular construct, suggesting that the motor domain of Myo7B may be a limiting factor in preventing targeting to basal filopodia. Together, these results indicate that the mode of dimerization along with the identity of the motor domain can guide actin track selection by members of MF myosins.

Sequences from the cargos ANKS4B and USH1G can support apical targeting of Myo7B

One of the binding partners of Myo7B within the IMAC is the scaffold ANKS4B. We recently identified a robust BB targeting sequence in ANKS4B that is essential for the scaffold to promote IMAC-mediated apical assembly of enterocytes (Graves *et al.*, 2020). This sequence targets to apical microvilli in an autonomous manner and does not directly interact with the other IMAC components. We termed this targeting sequence the "linker segment" (LK), as it links the highly conserved N-terminal ankyrin-repeat domain of ANKS4B to the central (CEN) domain that associates with Myo7B (Supplemental Figure S8A). The ANKS4B LK segment contains a highly predicted coiled-coil motif along with a putative membrane-binding basic-hydrophobic repeat sequence that are both required for its BB targeting ability. Studies with recombinant ANKS4B LK segment show that it behaves as an oligomer in vitro (Graves *et al.*, 2020). The targeting and oligomerization properties of the ANKS4B LK segment may make it an ideal candidate sequence within the IMAC that could support targeting of Myo7B to microvillar tips. To explore this, the ANKS4B LK segment was fused to a motor-neck fragment of Myo7B (Figure 8A; Myo7B-MN-4B LK) to assess whether this sequence could support Myo7B tip targeting, as seen with the GCN4 leucine zipper motif. Targeting of this construct was compared with full-length Myo7B, the isolated motor-neck of Myo7B with no GCN4 motif, and the forced dimer of Myo7B. Imaging the Myo7B-ANKS4B LK chimera revealed prominent targeting to apical microvilli (Figure 8, E and G). However, in most cases, this protein was found across the entire axis of microvilli and not exclusively at the distal tips (Figure 8E). This is likely due to the direct apical targeting ability of the ANKS4B LK segment that may "saturate" binding sites found in the microvilli when the chimera is expressed at high levels. In agreement with this, cells expressing lower amounts of the Myo7B-ANKS4B LK chimera appeared to have a signal that was more restricted to the distal tips (Supplemental Figure S8B; see arrows in the zoom panels), similar to what is seen with both full-length Myo7B (Figure 8B) and the Myo7B forced dimer (Figure 8D). In contrast, the isolated motor-neck fragment of Myo7B was predominately cytoplasmic (Figure 8, C and G).

The functional homolog of ANKS4B that operates in the Usher complex is the scaffold USH1G (Supplemental Figure S8A). While the USH1G LK segment does not exhibit the inherent ability to target to microvilli when expressed in CACO-2_{BBE} cells (Supplemental Figure S8, D and E), previous studies have shown that USH1G does oligomerize (Adato *et al.*, 2005; Sorusch *et al.*, 2017) and have partially mapped this property to a region of the scaffold that includes its LK segment (Supplemental Figure S8A). We fused the USH1G LK sequence to a motor-neck fragment of Myo7B (Figure 8A; Myo7B-MN-1G LK) to test whether it could support Myo7b targeting. Unlike

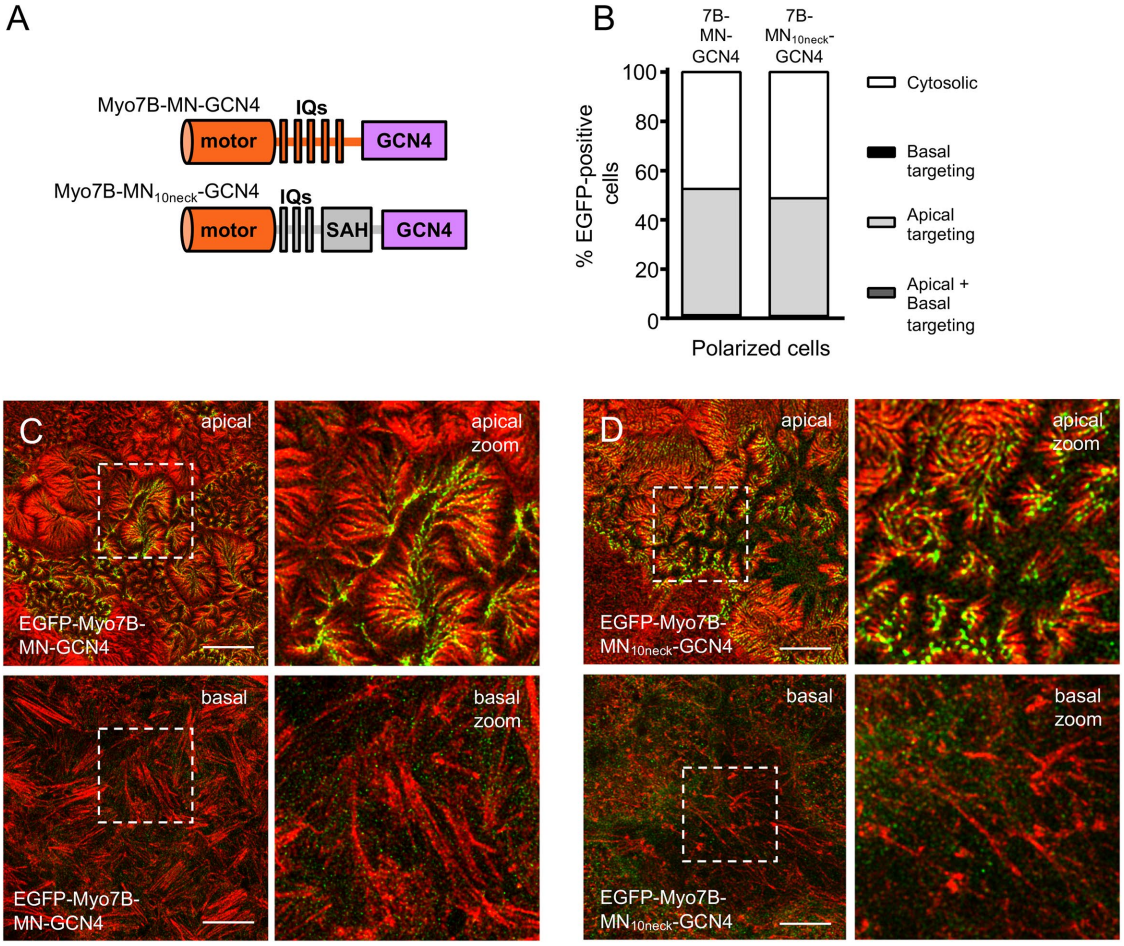

FIGURE 5: Lever arm identity does not dictate actin track selection of Myo7B expressed in polarized CACO-2_{BBE} cells. (A) Diagram of EGFP-fusion constructs that were used to assess the role of the lever arm in actin track selection of Myo7B. (B) Quantification of apical and basal targeting properties of EGFP-fusion constructs tested. Myo7B-MN-GCN4, $n = 76$ cells; Myo7B-MN_{10neck}-GCN4, $n = 82$ cells. Stacked bars indicate mean. (C, D) Confocal images of the apical (top panels) and basal regions (bottom panels) from a representative image stack of 12-d polarized CACO-2_{BBE} cells stably expressing EGFP-fusion constructs tested. Boxed regions denote areas in zoomed panels for each figure. Scale bars, 20 μm.

the Myo7B-ANKS4B LK chimera, the Myo7B-USH1G LK construct targeted to the distal tips of apical microvilli (Figure 8, F and G). Line-scan analysis comparing the relative distribution of these two chimeras across the microvillar axis clearly showed that the USH1G chimera was enriched toward the distal tips of microvilli, while the Myo7B-ANKS4B LK chimera localized across the entire axis of BB microvilli (Figure 8H). We interpret these results as suggesting that the oligomerization ability of the USH1G LK segment promotes apical targeting of the Myo7B-USH1G LK chimera in a manner similar to a GCN4 forced dimer. Furthermore, targeting of the Myo7B-ANKS4B LK chimera may be supported by both the oligomerization properties and the direct BB targeting ability of the ANKS4B LK sequence.

IMAC and Usher complex cargo sequences can re-encode the actin track usage of Myo10

We were curious to investigate whether the oligomerization properties of the LK segments could influence what type of actin track that Myo10 targeted to in polarized epithelial cells. We generated constructs in which the native coiled-coil of Myo10 was replaced with the isolated LK segments of ANKS4B (Figure 9A; Myo10-MN-4B LK) and USH1G (Figure 9A; Myo10-MN-1G LK) and tested their targeting. Both chimeras exhibited robust targeting to basal filopodia at the early confluency time point, displaying similar levels compared with the wild-type minimal Myo10 (Supplemental Figure S9, A–D). On polarization, Myo10-ANKS4B LK and Myo10-USH1G LK chimeras changed actin tracks and targeted to the BB, where they localized toward the distal tips of microvilli (Figure 9, B, C, and E). This was especially surprising for the Myo10-USH1G LK chimera, since the isolated USH1G LK segment does not exhibit the inherent ability to target to apical microvilli, unlike its counterpart found in ANKS4B (Supplemental Figure S8, C and D). We noted, however, that the Myo10-USH1G LK chimera did exhibit a lower level of targeting compared with the Myo10-ANKS4B LK construct, suggesting that the direct BB targeting ability of the ANKS4B LK segment likely contributes to robust tip targeting when fused to Myo10. In agreement with this, a motor-dead variant of the Myo10-ANKS4B LK chimera still exhibited partial targeting to apical microvilli, though it did not appear restricted to the distal tips (Figure 9D). In contrast, the same motor mutation completely abolished apical targeting of the Myo10-USH1G LK chimera (Figure 9F). Although basal filopodia targeting of these chimeras was substantially reduced in polarized

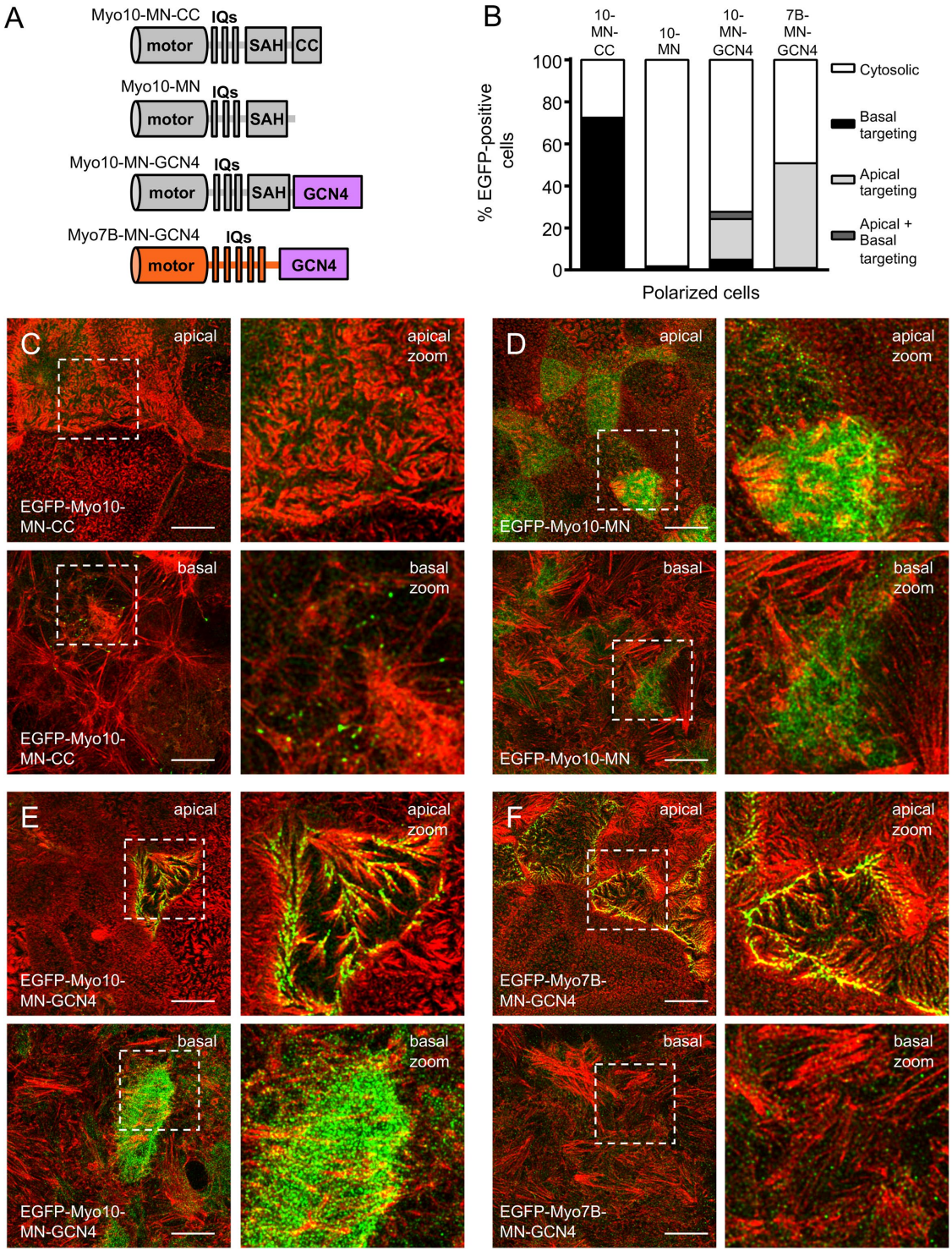

FIGURE 6: Parallel dimerized Myo10 utilizes apical microvilli as an actin track in polarized CACO-2_{BBE} cells. (A) Diagram of EGFP-fusion constructs that were used to assess the role of the mode of dimerization on actin track selection by Myo10. (B) Quantification of apical and basal targeting properties of EGFP-fusion constructs tested. Myo10-MN-CC, $n = 118$ cells; Myo10-MN, $n = 115$ cells; Myo10-MN-GCN4, $n = 103$ cells; Myo7B-MN-GCN4, $n = 105$ cells. Bars indicate mean ± SD. (C–F) Confocal images of the apical (top panels) and basal regions (bottom panels) from a representative image stack of 12-d polarized CACO-2_{BBE} cells stably expressing EGFP-fusion constructs tested. Boxed regions denote areas in zoomed panels for each figure. Scale bars, 20 μm.

cells, it was not completely absent. Distinct examples of residual filopodia targeting could be observed in cells also exhibiting prominent apical targeting (Supplemental Figure S9E; see arrows in the basal zoom panel). These results demonstrate that oligomeric sequences from the IMAC and Usher complex cargo molecules, ANKS4B and USH1G, respectively, have the ability to bias actin

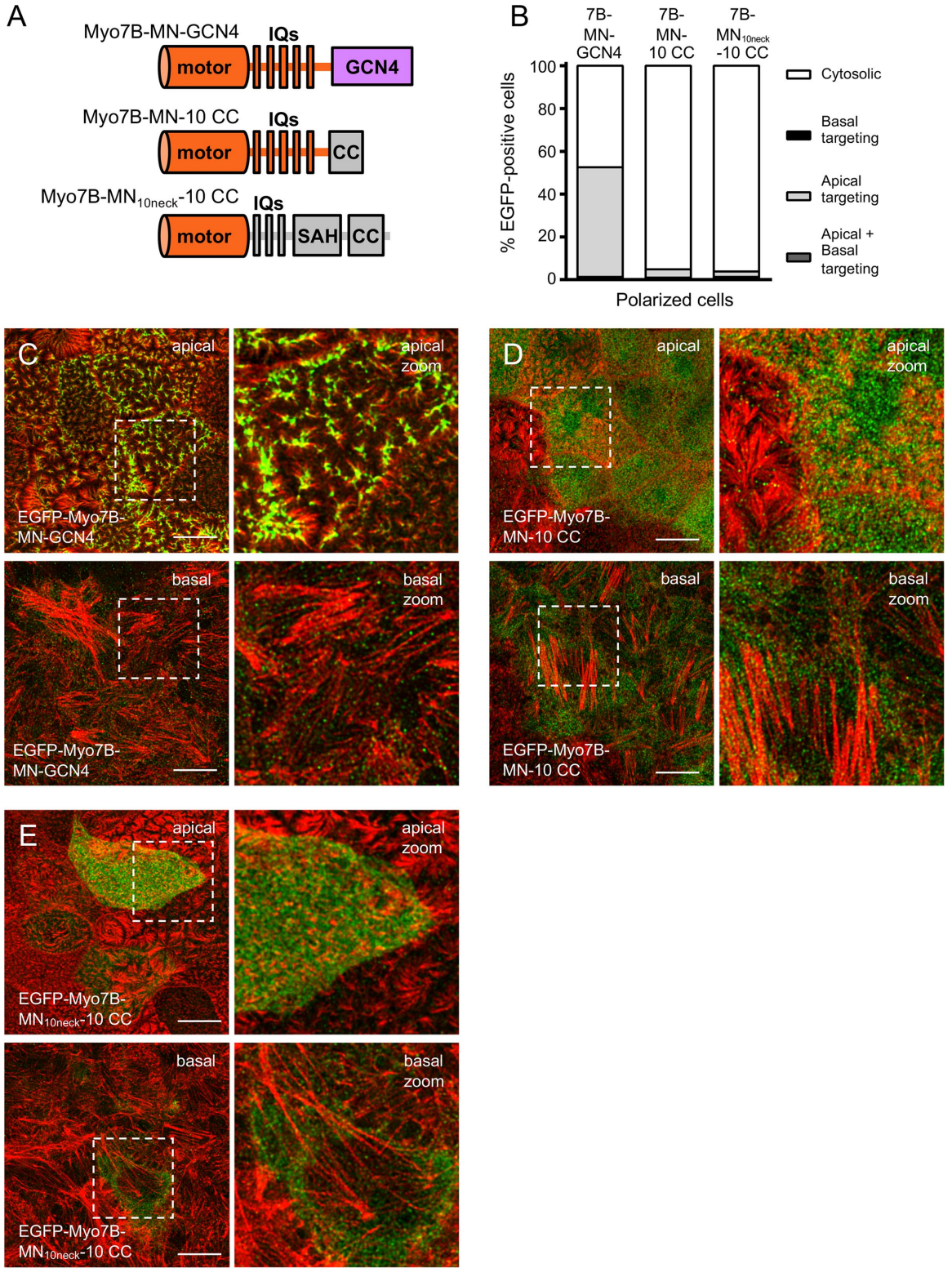

FIGURE 7: Antiparallel dimerization of Myo7B does not support apical or basal targeting in polarized CACO-2_{BBE} cells. (A) Diagram of EGFP-fusion constructs that were used to assess influence of the mode of dimerization on Myo7B targeting in CACO-2_{BBE} cells. (B) Quantification of apical and basal targeting properties of EGFP-fusion constructs tested. Myo7B-MN-GCN4, $n = 76$ cells; Myo7B-MN-10 CC, $n = 89$ cells; Myo7B-MN_{10neck}-10 CC, $n = 71$ cells. Stacked bars indicate mean. (C–E) Confocal images of the apical (top panels) and basal regions (bottom panels) from a representative image stack of 12-d polarized CACO-2_{BBE} cells stably expressing EGFP-fusion constructs tested. Boxed regions denote areas in zoomed panels for each figure. Scale bars, 10 μm.

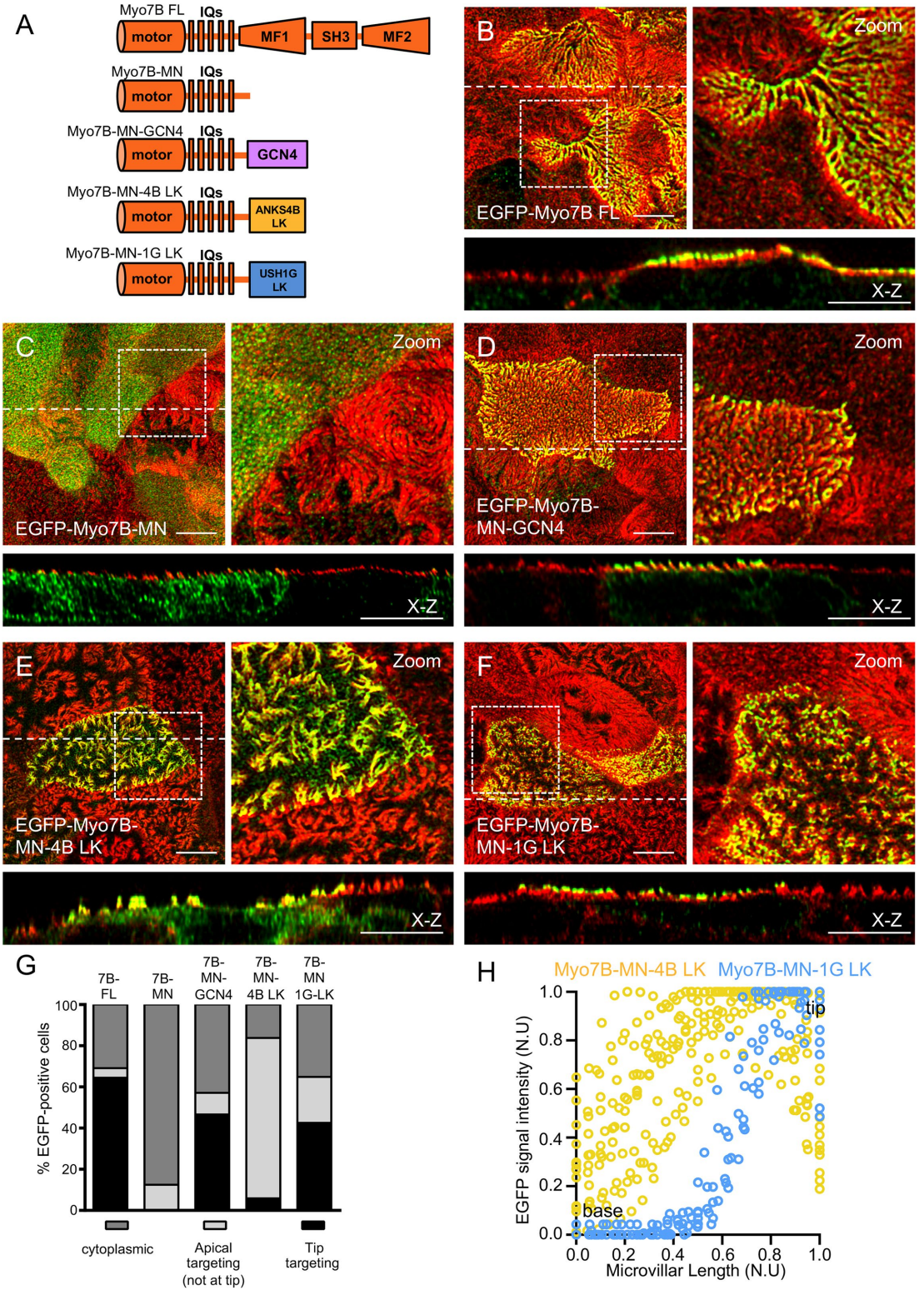

FIGURE 8: The LK segments of ANKS4B and USH1G support apical targeting of Myo7B in CACO-2_{BBE} cells. (A) Diagram of constructs used to assess the ability of the ANKS4B and USH1G LK segments to support Myo7B targeting. (B–F) Confocal images of 12-d polarized CACO-2_{BBE} cells stably expressing EGFP-fusion constructs tested. Boxed regions denote areas in zoomed panels for each figure. Dashed lines indicate the position where X-Z sections were taken; X-Z sections are shown below each en face image. Scale bars, 10 μm. (G) Quantification of targeting properties of the EGFP-fusion constructs tested. Myo7B FL, $n = 67$ cells; Myo7B-MN, $n = 82$ cells; Myo7B-MN-GCN4, $n = 54$ cells; Myo7B-MN-4B LK, $n = 84$ cells; Myo7B-MN-1G LK, $n = 73$ cells. Stacked bars indicate mean. (H) Line-scan analysis of EGFP-Myo7B-MN-4B LK (yellow) and EGFP-Myo7B-MN-1G LK (blue) signal intensity collected parallel to the microvillar axis in stably transduced CACO-2_{BBE} cells. Microvillar length has been normalized, where 0 = base of microvilli and 1 = distal tip of microvilli. N.U = normalized units.

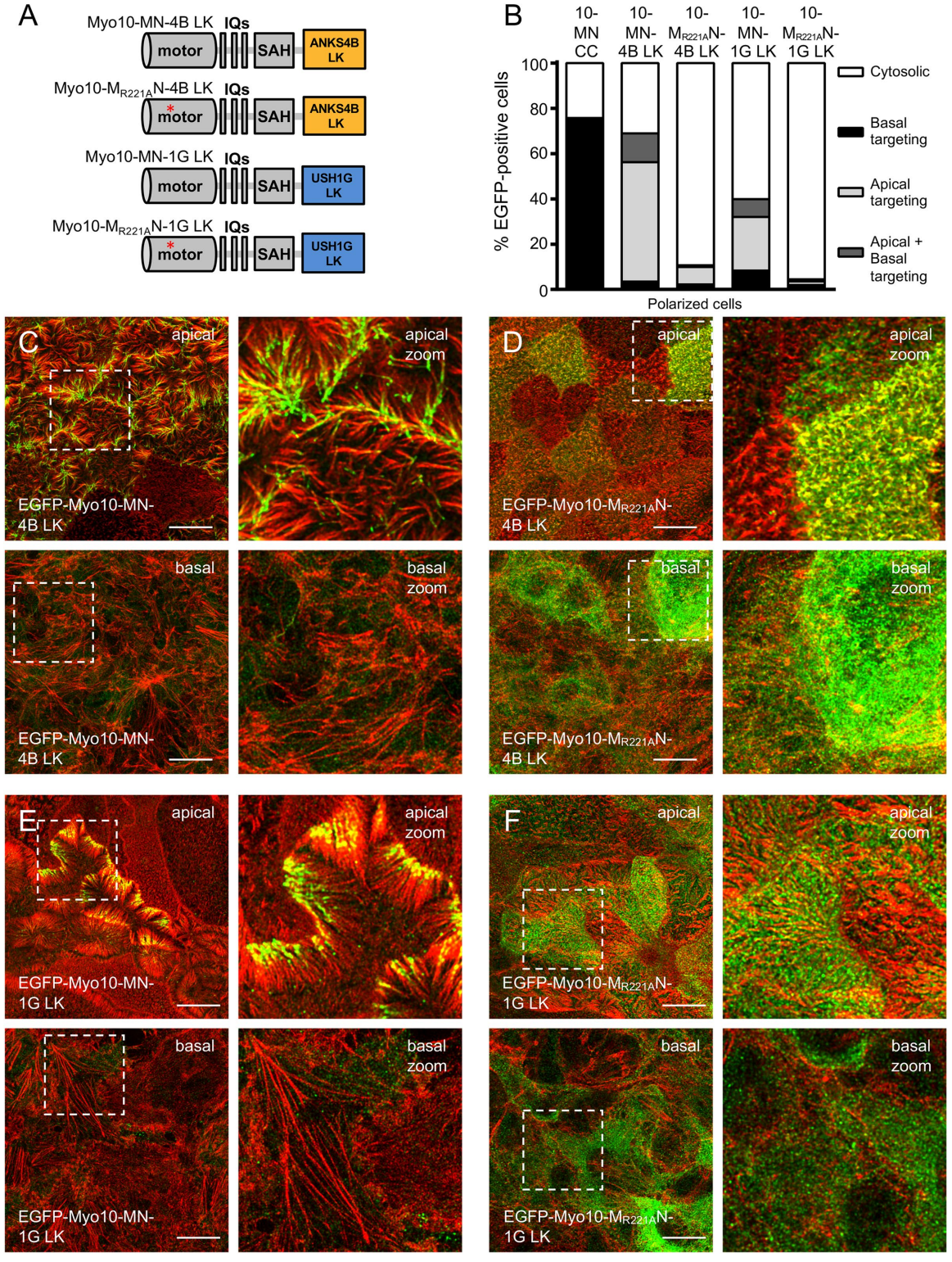

FIGURE 9: Fusion of the ANKS4B and USH1G LK segments to a motor-neck fragment of Myo10 re-encodes actin track selection to target the myosin to apical microvilli in polarized CACO-2_{BBE} cells. (A) Diagram of constructs used to assess the ability of ANKS4B and USH1G LK segments to re-encode actin track selection of Myo10. (B) Quantification of apical and basal targeting properties of EGFP-fusion constructs tested. Myo10-MN-4B LK, $n = 106$ cells; Myo10-M_{R221A}N-4B LK, $n = 114$ cells; Myo10-MN-1G LK, $n = 113$ cells; Myo10-M_{R221A}N-1G LK, $n = 107$ cells. Bars indicate mean ± SD. (C–F) Confocal images of the apical (top panels) and basal regions (bottom panels) from a representative image stack of 12-d polarized CACO-2_{BBE} cells stably expressing EGFP-fusion constructs tested. Boxed regions denote areas in zoomed panels for each figure. Scale bars, 10 μm.

track selection of a myosin toward apical microvilli in polarized epithelial cells.

DISCUSSION

We were struck by the observation that members of the MF myosin family are able to select between distinct parallel-bundled actin networks that can coexist in cells, even in the absence of information from their cargo-binding tail domains.

We undertook this study to begin to define the sequence features of these myosins that impart this ability (see Supplemental Table S1 for a summary of constructs used in this study and their targeting properties). Our results support the idea that the geometry of the lever arms of a dimerized myosin, which largely influences the distance that can be achieved between the two motor heads during stepping, plays a significant role in determining the type of actin network a myosin can utilize. We observed that the native antiparallel coiled-coil of Myo10 biases this motor toward trafficking on basal filopodia, while being incompatible with trafficking on the actin network found in apical microvilli. In contrast, artificially dimerizing Myo10 with a GCN4 parallel coiled-coil allowed for targeting to both filopodia and apical microvilli. Recent in vitro studies have demonstrated that the specific oligomerization sequence associated with Myo10 influences how the motor behaves toward different types of actin (Caporizzo *et al.*, 2018). Native antiparallel Myo10 dimers exhibited selective processivity on fascin-bundled actin, while artificial parallel Myo10 dimers trafficked on both bundled actin and single actin filaments. One possibility is that differences in the actin bundle architecture between microvilli and filopodia prevent native antiparallel dimerized Myo10 from using microvilli as a track. Electron tomography studies of microvillar actin bundles show that their actin filaments do not lie exactly parallel to each other; instead, they are twisted in a clockwise coil with a pitch of ~120°/μm (Ohta *et al.*, 2012). This may arrange myosin binding sites on adjacent actin filaments in a configuration that supports the reach of a parallel dimer of Myo10, but is not optimal for an antiparallel dimerized motor. In agreement with this bias, Myo7B microvillar targeting was not supported by the antiparallel coiled-coil from Myo10, while parallel dimerization of Myo7B by a GCN4 leucine zipper promoted robust apical targeting. Strikingly, we did not observe Myo7B targeting to filopodia under any circumstances. This begs the question of how Myo7B becomes restricted against utilizing filopodia as a track, given that we saw significant targeting of the Myo10-GCN4 chimera on basal protrusions. The identity of the motor domain may also play a role in biasing a particular myosin toward a specific actin track that has a distinct composition of actin-binding proteins and exhibits different dynamics. Studies have shown that the motor domain of Myo5a is sensitive to the specific isoform of tropomyosin that decorates actin filaments, suggesting that actin-associated proteins can influence actin track selection behavior by a myosin (Sckolnick *et al.*, 2016). It is important to note, however, that there are examples of Class 7 myosins from other species that exhibit tracking to the tips of filopodialike protrusions. A forced dimer of Drosophila Myo7A motor-neck induces filopodia and tracks to their tips in Drosophila S2 cells (Liu *et al.*, 2021), similar to the single Class 7 myosin found in Dictyostelium that creates and tracks to the tips of filopodialike protrusions in the social amoebae (Arthur *et al.*, 2019). Going forward, it may be informative to express these examples of Class 7 myosins along with their cognate light chains in an epithelial cell system to observe whether they exhibit motility and assess what type of actin network they are biased toward. Furthermore, modulating the properties of basal filopodia by expressing BB-specific actin cross-linking proteins in fibroblastlike cells in an attempt to reconstitute motility of the vertebrate Class 7 myosins will also likely shed light on how actin bundle structure may influence myosin recruitment.

Cargo is proposed to mediate oligomerization of the Class 7 myosins, allowing these motors to traffic on actin structures (Siththanandan and Sellers, 2011). A recent study of Drosophila Myo7A and its binding partner M7BP revealed that they predominately formed a 2:2 stochiometric complex to become processive both in vitro and in cells (Liu *et al.*, 2021). We previously identified an oligomeric apical targeting sequence found in ANKS4B that lies directly upstream of the Myo7B-binding domain in this scaffold (Graves *et al.*, 2020). We show here that when fused to a motor-neck fragment of Myo7B, the ANKS4B LK segment promoted apical targeting of the myosin. A similar construct using the USH1G LK segment (which lacks the inherent ability to target to the BB) accumulated at the tips of apical microvilli. The LK sequences from ANKS4B and USH1G were also able to support Myo10 targeting to the tips of filopodia and apical microvilli, similar to a GCN4 parallel dimerization sequence. Although our results suggest that the LK segments from these scaffolds can support motility of a myosin, it is currently unclear whether these sequences are directly responsible for promoting the active, oligomeric form of Myo7A or Myo7B within their respective adhesion complex. It is interesting to note that the targeting ability of the LK segment of ANKS4B appears to be tightly regulated in the context of the full-length protein. Activation of the LK segment apical targeting properties within ANKS4B is dependent on its interaction with the other IMAC scaffold USH1C (Crawley *et al.*, 2016). This is likely a mechanism to ensure that ANKS4B only becomes active when associated with its correct binding partners. Future studies investigating whether activation of ANKS4B by USH1C also promotes the oligomerization of the ANKS4B LK segment along with its BB targeting ability will yield important information. One can envision an elegant mechanism in which combining apical targeting and oligomerization properties into a single sequence in an IMAC scaffold that is under tight regulation could contribute to both the correct temporal assembly and the spatial positioning of the IMAC at the distal tips of BB microvilli by forming an active motor–cargo complex.

MATERIALS AND METHODS

Request a protocol through *Bio-protocol*.

Molecular biology

The human cDNA constructs used in this study are as follows: ANKS4B, GI: 1519246130, UniProtKB-Q8N8V4; Myo7A, GI: 1519245357, UniProtKB-Q13402; Myo7B, GI: 122937511, UniProtKB-Q6PIF6; USH1G, GI: 1519473545, UniProtKB-Q495M9. The bovine Myo10 cDNA construct used in this study was GI: 1755048, UniProtKB-P79114. DNA encoding these components were generated by PCR and TOPO cloned into the pCR8 entry vector (Invitrogen). All constructs were verified by sequencing. Domain boundaries and the design of constructs were guided by information from Uniprot and past studies, especially when structural data were available (Lu *et al.*, 2012; Ropars *et al.*, 2016; Li *et al.*, 2017a). The domain boundaries for Myo7B used are as follows: Myo7B-MN (aa 1–968), Myo7B full-length tail (aa 923–2116). The domain boundaries for the Myo7A constructs used are as follows: Myo7A-MN (aa 1–1014), Myo7A-MN$_{\Delta SAH}$-GCN4 (aa 1–876), Myo7A-MN$_{\Delta IQ}$-GCN4 (aa 1–1014, Δ742–849), Myo7A full-length tail (aa 1017–2215). The domain boundary for the ANKS4B and USH1G constructs are as follows: ANKS4B LK (aa 119–252) and USH1G LK (aa 120–294). The domain boundaries for the Myo10 constructs used are as follows: Myo10-MN-CC (aa 1–944), Myo10-MN (aa 1–876), and

Myo10-MNΔSAH (aa 1–944; Δ814–861). For Myo7B oligomerization chimeras, a motor-neck fragment of Myo7B (aa 1–968) was fused in frame using a small connecting sequence (connecting sequence is in boldfaceand underlined) to a GCN4 leucine zipper motif (….DVDGLSTMKQLE….) to generate Myo7B-MN-GCN4, and the ANKS4B LK segment (130–252;….DVDGLRGKKVTR….) and USH1G LK segment (130–294; ….DVDGLRGKLVGK…..) to generate Myo7B-MN-4B LK and Myo7B-MN-1G LK, respectively. A motor-neck fragment of Myo7A (aa 1–1014) was fused in frame to a GCN4 leucine zipper motif to generate Myo7A-MN-GCN4 (….QGTTT-GSTGSRMKQLED….). A motor-neck fragment of Myo10 (aa 1–890) was fused in frame to a GCN4 leucine zipper motif to generate Myo10-MN-GCN4 (….KQVEETSMKQLED….). The motor domain of Myo7B (aa 1–754) was fused in frame to the neck and coiled-coil motif of Myo10 (aa 734–944; no connecting sequence was necessary) to generate Myo7B-MN_{10neck}-10 CC. A motor-neck domain of Myo7B (aa 1–968) was fused in frame to the coiled-coil domain of Myo10 (aa 879–944; ….DVDGLRGLEKQK….) to generate Myo7B-MN-10 CC. The lever arm of Myo7B (aa 752–884) replaced the IQ motifs of Myo10 (aa 1–893; replaced aa 731–812) to generate Myo10-MN_{7BIQs}-CC. The lever arm of Myo7B (aa 752–884) replaced the IQ motifs and SAH motif of Myo10 (aa 1–893; replaced aa 731–861) to generate Myo10-MN_{7BIQs}-ΔSAH-CC. All constructs were expressed using the pINDUCER20 EGFP-C1 vector (Crawley *et al.*, 2016), which tags EGFP to the N-terminus of the protein and utilizes the inducible TRE2 promoter to drive expression. Cloning into this vector results in generation of a connecting sequence (SGLRSRIT-SLYKKAGSEFAL) between the end of EGFP and the starting methionine of the construct. The KD shRNA clones targeting Myo7B were expressed in the pLKO.1vector and has been previously validated in CACO-2_{BBE} cells (Weck *et al.*, 2016). These constructs correspond to TRC clones TRCN0000247713 and TRCN0000247715 (Open Biosystems). Point mutations were introduced into constructs using the QuikChange site-directed mutagenesis kit (Agilent, Cat#200523).

Cell culture, lentivirus production, and stable cell line generation

CACO-2_{BBE} and HEK293FT cells were cultured at 37°C and 5% CO_2 in a humidified incubator using DMEM with high glucose and 2 mM L-glutamine. Medium was supplemented with 20% fetal bovine serum (FBS) for CACO-2_{BBE} cells and 10% FBS for HEK293FT cells. All CACO-2_{BBE} cell lines within this study were generated by stable selection of lentiviral transduced cultures. Lentivirus particles were generated by cotransfecting HEK293FT cells (10-cm dish at 80% confluency) with 6 µg of lentiviral overexpression plasmid with 4 µg psPAX2 packaging plasmid and 0.8 µg pMD2.G envelope plasmid using polyethylenimine reagent (Polysciences). Cells were incubated with transfection medium for 12 h, after which they were exchanged with fresh medium. Cells were subsequently incubated for 2 d to allow for lentiviral production into the medium. Medium containing lentiviral particles was collected and filtered with a 0.45-µm syringe filter. Lentiviral particles were concentrated and recovered using with Lenti-X concentrator reagent according to the recommended protocol (Takara). For lentivirus transduction, CACO-2_{BBE} cells were grown to 90% confluency in T25 flasks. The medium was then supplemented with 8 µg/ml polybrene after which ~300 µl of concentrated lentiviral particle solution was added. After 12 h of incubation with lentivirus, the cells were reseeded into 10-cm dishes and grown for 3 d. Cells were then reseeded into T182 flasks with medium containing 50 µg/ml puromycin or 1 mg/ml G418 and passaged to select for stable integration. Induction of pINDUCER20 EGFP constructs was driven by including 1 µg/ml doxycycline in the media.

Microscopy

Samples were imaged using a Leica SP8 laser-scanning confocal microscope equipped with HyVolution deconvolution software. CACO-2_{BBE} monolayers were washed once in warm phosphate-buffered saline (PBS) and incubated briefly with 0.02% Saponin (Sigma) in warm PBS, then fixed for 15 min with 4% paraformaldehyde in warm PBS containing 0.1% Triton X-100 (Sigma). After fixation, cells were washed three times with warm PBS and blocked overnight in 5% bovine serum albumin solution. Immunostaining was performed using anti-Myo7B (1:25; Sigma Cat#HPA039131) or anti-GFP (1:200; Aves Labs Cat#GFP1020) primary antibodies at 37°C for 2 h. Coverslips were washed three times with warm PBS and incubated for 1 h with Alexa Fluor-488 donkey anti-rabbit or Alexa Fluor-488 goat anti-chicken (1:200) secondary antibodies (where appropriate) along with Alexa Fluor-568 Phalloidin (1:200). Coverslips were then washed five times in PBS and mounted with Prolong Diamond anti-fade reagent (Invitrogen). Images shown are either en face maximum projections through the full height of the BB or maximum projections encompassing the basal membrane marked by the stress fibers, with the exception of X-Z sections, which are single plane confocal images. Paraffin-embedded mouse intestinal tissue sections were deparaffinized using Histo-clear II solution (Fisher), rehydrated in a descending graded ethanol series, and stained using anti-Myo7B (1:25; Sigma Cat#HPA039131) or anti-Myo7A (1:200; Proteintech Cat#20720-1-AP) along with anti-Villin (1:50; Santa Cruz Cat#sc-58897), followed by Alexa Fluor-488 donkey anti-rabbit (1:200; Invitrogen) and Alexa Fluor-568 donkey anti-mouse (1:200; Invitrogen). Sections were then dehydrated in an ascending graded ethanol series and mounted with Prolong Diamond anti-fade (Invitrogen).

Analysis of microvillar clustering in CACO-2_{BBE} cells

Scramble, Myo7B KD, and Myo7B KD-rescue CACO-2_{BBE} stable cell lines were allowed to polarize for 12 d on coverslips after reaching confluency and were subsequently stained for F-actin and Myo7B (scramble and KD cell lines) or EGFP (KD-rescue cell lines). Individual cells were scored according to whether they exhibited nonclustering microvilli or microvillar clustering (i.e., possessing one or more distinct clusters of five or more microvilli). For rescue cell lines, only EGFP-positive cells were scored. Data were analyzed in a blinded manner.

Image analysis

Image analysis was performed using ImageJ (National Institutes of Health [NIH]). For analysis of relative targeting, we calculated the ratio of BB to cytosolic signal intensity as previously described (Crawley *et al.*, 2014b). Ratios at or below 1.2 were considered nontargeting, while those above 1.2 were considered to have apical targeting. Cells exhibiting apical targeting were then assessed for the distribution of the EGFP signal along the axis of microvilli using line-scan analysis. For line-scan signal analysis of X-Z sections or tissue cross-sections, a line was drawn through the BB oriented parallel to the microvillar axis as judged by the F-actin signal. The intensity of the EGFP channel along that line was subsequently recorded and normalized to the maximum grayscale value for an 8-bit image (i.e., 255). The corresponding positions for each intensity value was normalized so that the base of the microvillus was equal to 0 and the tip was equal to 1. Normalized line scans were then plotted together and fit to a single Gaussian using nonlinear regression (Prism v.6, GraphPad), which revealed the position of peak signal intensity and distribution width (SD) relative to the microvillar axis. Constructs displaying a peak signal position of 0.8 or above were considered tip

targeted. Assessment of basal targeting was performed by first limiting the Z-stack to the basal region, as judged by the appearance of abundant stress fibers. Targeting to the basal region was assessed using a maximum projection image of the basal stacks, in which EGFP-positive cells exhibiting 3+ EGFP puncta above a set threshold (see below for thresholding procedure) were considered to have basal targeting. Data were analyzed in a blinded manner.

Analysis of basal targeting in CACO-2_{BBE} cells

For CACO-2_{BBE} cells, stable cell lines were plated at ~20% confluency on coverslips housed in 6-well dishes and allowed to adhere and polarize for ~1–2 d for early confluency samples and for 12 d for the polarized time point. Data were collected from fields of view that were 91.2 µm × 91.2 µm in size, with the image stack encompassing the full height of the cells across the monolayer. Stacks were then limited to the basal region, as judged by the appearance of abundant stress fibers. Maximum projection images of basal stacks were processed by setting signal threshold for the EGFP channel between 15,000 and 65,535 for the 16-bit image. Signal was then detected using the "Analyze Particles" function in ImageJ, with a minimum cut-off size value of 0.05 µm and a circularity range set to 0–1. Targeting was expressed as the number of EGFP puncta detected per 10,0000 μm^2. The percentage of cells expressing EGFP signal was determined by counting EGFP-positive cells across 15 fields of view and was used to normalize between samples to account for minor differences among expression levels between different stable cell lines. Data were analyzed in a blinded manner.

Immunoblot analysis

For analysis of CACO-2_{BBE} KD cell lines, monolayers were allowed to polarize for 21 d after which cells were washed once in PBS, recovered by a cell scraper, and frozen for storage at –80°C. Cells were thawed on ice; resuspended in ice-cold CelLytic M buffer (Sigma) containing 2 mM ATP, 1× cOmplete ULTRA protease inhibitor cocktail (Roche), and 1 mM Pefabloc SC (Roche); and lysed by several rounds of needle aspiration (27G × 11/4 needle). Cell lysates were centrifuged at 16,000 × *g* and the soluble material was recovered. Protein samples were separated on 4–12% Bis-Tris gels (Novex) and immunoblot analysis was performed using the following antibody dilutions, anti-Myo7B (1:100; Sigma Cat#HPA039131) and anti-GAPDH (1:10,000; Proteintech Cat#60004), and used for immunoblot analysis. Immunostaining was performed using anti-Myo7B (1:25; Sigma Cat#HPA039131). For analysis of mouse intestinal tissue samples, ~2-mm^2 tissue sections were dissected from a mouse duodenum and immediately homogenized using a Dounce tissue grinder in ice-cold CelLytic M buffer (Sigma) containing 2 mM ATP, 1× cOmplete ULTRA protease inhibitor cocktail (Roche), and 1 mM Pefabloc SC (Roche). Tissue lysates were centrifuged at 16,000 × *g* and the soluble material was recovered. Protein samples were separated on 4–12% Bis-Tris gels (Novex) and immunoblot analysis was performed using the following antibody dilutions: anti-Myo7B (1:100; Sigma Cat#HPA039131), anti-Myo7A (1:200; Proteintech Cat#20720-1-AP), and anti-GAPDH (1:100; Proteintech Cat#60004).

Statistical analysis

All graphs were generated and statistical analyses were performed using Prism v.6 (GraphPad). For all figures, error bars represent SD. Unpaired two-tailed *t* tests were employed to determine statistical significance between reported values. For all experiments, data were from three independent immunostaining experiments from stable cell lines that were independently derived twice.

DATA AVAILABILITY

All data are found within the paper.

ACKNOWLEDGMENTS

We thank all members of the Crawley laboratory for advice and support. This work was supported by the Northern Ohio Alliances for Graduate Education and the Professoriate (NOA-AGEP) fellowship (M.J.G.), First Year Summer Research Experience (FYSRE) and Undergraduate Summer Research and Creative Activities Program (USR-CAP) University of Toledo scholarships (Z.A.S. and R.A.E.), University of Toledo Start-up funds, and NIH R15GM131382 (S.W.C.).

REFERENCES

Adato A, Michel V, Kikkawa Y, Reiners J, Alagramam KN, Weil D, Yonekawa H, Wolfrum U, El-Amraoui A, Petit C (2005). Interactions in the network of Usher syndrome type 1 proteins. Hum Mol Genet 14, 347–356.

Arthur AL, Songster LD, Sirkia H, Bhattacharya A, Kikuti C, Borrega FP, Houdusse A, Titus MA (2019). Optimized filopodia formation requires myosin tail domain cooperation. Proc Natl Acad Sci USA 116, 22196–22204.

Baboolal TG, Sakamoto T, Forgacs E, White HD, Jackson SM, Takagi Y, Farrow RE, Molloy JE, Knight PJ, Sellers JR, Peckham M (2009). The SAH domain extends the functional length of the myosin lever. Proc Natl Acad Sci USA 106, 22193–22198.

Bartles JR, Zheng L, Li A, Wierda A, Chen B (1998). Small espin: a third actin-bundling protein and potential forked protein ortholog in brush border microvilli. J Cell Biol 143, 107–119.

Bement WM, Hasson T, Wirth JA, Cheney RE, Mooseker MS (1994). Identification and overlapping expression of multiple unconventional myosin genes in vertebrate cell types [correction published in Proc Natl Acad Sci USA 91, 6549–6553.

Berg JS, Cheney RE (2002). Myosin-X is an unconventional myosin that undergoes intrafilopodial motility. Nat Cell Biol 4, 246–250.

Bretscher A, Weber K (1979). Villin: the major microfilament-associated protein of the intestinal microvillus. Proc Natl Acad Sci USA 76, 2321–2325.

Bretscher A, Weber K (1980). Fimbrin, a new microfilament-associated protein present in microvilli and other cell surface structures. J Cell Biol 86, 335–340.

Caporizzo MA, Fishman CE, Sato O, Jamiolkowski RM, Ikebe M, Goldman YE (2018). The Antiparallel Dimerization of Myosin X Imparts Bundle Selectivity for Processive Motility. Biophys J 114, 1400–1410.

Chen ZY, Hasson T, Kelley PM, Schwender BJ, Schwartz MF, Ramakrishnan M, Kimberling WJ, Mooseker MS, Corey DP (1996). Molecular cloning and domain structure of human myosin-VIIa, the gene product defective in Usher syndrome 1B. Genomics 36, 440–448.

Chen ZY, Hasson T, Zhang DS, Schwender BJ, Derfler BH, Mooseker MS, Corey DP (2001). Myosin-VIIb, a novel unconventional myosin, is a constituent of microvilli in transporting epithelia. Genomics 72, 285–296.

Choi MS, Graves MJ, Matoo S, Storad ZA, El Sheikh Idris RA, Weck ML, Smith ZB, Tyska MJ, Crawley SW (2020). The small EF-hand protein CALML4 functions as a critical myosin light chain within the intermicrovillar adhesion complex. J Biol Chem 295, 9281–9296.

Chou SW, Hwang P, Gomez G, Fernando CA, West MC, Pollock LM, Lin-Jones J, Burnside B, McDermott BM Jr (2011). Fascin 2b is a component of stereocilia that lengthens actin-based protrusions. PLoS One 6, e14807.

Crawley SW, Mooseker MS, Tyska MJ (2014a). Shaping the intestinal brush border. J Cell Biol 207, 441–451.

Crawley SW, Shifrin DA Jr, Grega-Larson NE, McConnell RE, Benesh AE, Mao S, Zheng Y, Zheng QY, Nam KT, Millis BA, *et al.* (2014b). Intestinal brush border assembly driven by protocadherin-based intermicrovillar adhesion. Cell 157, 433–446.

Crawley SW, Weck ML, Grega-Larson NE, Shifrin DA Jr, Tyska MJ (2016). ANKS4B Is Essential for Intermicrovillar Adhesion Complex Formation. Dev Cell 36, 190–200.

Francis SP, Krey JF, Krystofiak ES, Cui R, Nanda S, Xu W, Kachar B, Barr-Gillespie PG, Shin JB (2015). A short splice form of Xin-actin binding repeat containing 2 (XIRP2) lacking the Xin repeats is required for maintenance of stereocilia morphology and hearing function. J Neurosci 35, 1999–2014.

Graves MJ, Matoo S, Choi MS, Storad ZA, El Sheikh Idris RA, Pickles BK,Acharya, P, Shinder PE, Arvay TO, Crawley SW (2020). A cryptic sequence targets the adhesion complex scaffold ANKS4B to apical

microvilli to promote enterocyte brush border assembly. J Biol Chem 295, 12588–12604.
Heissler SM, Sellers JR (2016). Kinetic adaptations of myosins for their diverse cellular functions. Traffic 17, 839–859.
Houdusse A, Titus MA (2021). The many roles of myosins in filopodia, microvilli and stereocilia. Curr Biol 31, R586–R602.
Kitajiri S, Sakamoto T, Belyantseva IA, Goodyear RJ, Stepanyan R, Fujiwara I, Bird JE, Riazuddin S, Riazuddin S, Ahmed ZM, *et al.* (2010). Actin-bundling protein TRIOBP forms resilient rootlets of hair cell stereocilia essential for hearing. Cell 141, 786–798.
Li J, Chen Y, Deng Y, Unarta IC, Lu Q, Huang X, Zhang M (2017a). Ca2+-Induced rigidity change of the myosin VIIa IQ motif-single alpha helix lever arm extension. Structure 25, 579–591.e574.
Li J, He Y, Weck ML, Lu Q, Tyska MJ, Zhang M (2017b). Structure of Myo7b/USH1C complex suggests a general PDZ domain binding mode by MyTH4-FERM myosins. Proc Natl Acad Sci USA 114, E3776–E3785.
Liu KC, Jacobs DT, Dunn BD, Fanning AS, Cheney RE (2012). Myosin-X functions in polarized epithelial cells. Mol Biol Cell 23, 1675–1687.
Liu R, Billington N, Yang Y, Bond C, Hong A, Siththanandan V, Takagi Y, Sellers JR (2021). A binding protein regulates myosin-7a dimerization and actin bundle assembly. Nat Commun 12, 563.
Lu Q, Ye F, Wei Z, Wen Z, Zhang M (2012). Antiparallel coiled-coil-mediated dimerization of myosin X. Proc Natl Acad Sci USA 109, 17388–17393.
Matsudaira P, Mandelkow E, Renner W, Hesterberg LK, Weber K (1983). Role of fimbrin and villin in determining the interfilament distances of actin bundles. Nature 301, 209–214.
McConnell RE, Benesh AE, Mao S, Tabb DL, Tyska MJ (2011). Proteomic analysis of the enterocyte brush border. Am J Physiol Gastrointest Liver Physiol 300, G914–G926.
Mooseker MS, Graves TA, Wharton KA, Falco N, Howe CL (1980). Regulation of microvillus structure: calcium-dependent solation and cross-linking of actin filaments in the microvilli of intestinal epithelial cells. J Cell Biol 87, 809–822.
Nagy S, Ricca BL, Norstrom MF, Courson DS, Brawley CM, Smithback PA, Rock RS (2008). A myosin motor that selects bundled actin for motility. Proc Natl Acad Sci USA 105, 9616–9620.
Ohta K, Higashi R, Sawaguchi A, Nakamura K (2012). Helical arrangement of filaments in microvillar actin bundles. J Struct Biol 177, 513–519.
Peterson MD, Mooseker MS (1993). An in vitro model for the analysis of intestinal brush border assembly. I. Ultrastructural analysis of cell contact-induced brush border assembly in Caco-2BBe cells. J Cell Sci 105, 445–460.
Planelles-Herrero VJ, Blanc F, Sirigu S, Sirkia H, Clause J, Sourigues Y, Johnsrud DO, Amigues B, Cecchini M, Gilbert SP, *et al.* (2016). Myosin MyTH4-FERM structures highlight important principles of convergent evolution. Proc Natl Acad Sci USA 113, E2906–E2915.
Ropars V, Yang Z, Isabet T, Blanc F, Zhou K, Lin T, Liu X, Hissier P, Samazan F, Amigues B, *et al.* (2016). The myosin X motor is optimized for movement on actin bundles. Nat Commun 7, 12456.
Sakai T, Jung HS, Sato O, Yamada MD, You DJ, Ikebe R, Ikebe M (2015). Structure and regulation of the movement of human myosin VIIA. J Biol Chem 290, 17587–17598.
Sakai T, Umeki N, Ikebe R, Ikebe M (2011). Cargo binding activates myosin VIIA motor function in cells. Proc Natl Acad Sci USA 108, 7028–7033.
Sato O, Komatsu S, Sakai T, Tsukasaki Y, Tanaka R, Mizutani T, Watanabe TM, Ikebe R, Ikebe M (2017). Human myosin VIIa is a very slow processive motor protein on various cellular actin structures. J Biol Chem 292, 10950–10960.
Scheffer DI, Zhang DS, Shen J, Indzhykulian A, Karavitaki KD, Xu YJ, Wang Q, Lin JJ, Chen ZY, Corey DP (2015). XIRP2, an actin-binding protein essential for inner ear hair-cell stereocilia. Cell Rep 10, 1811–1818.
Sckolnick M, Krementsova EB, Warshaw DM, Trybus KM (2016). Tropomyosin isoforms bias actin track selection by vertebrate myosin Va. Mol Biol Cell 27, 2889–2897.
Sekerkova G, Zheng L, Mugnaini E, Bartles JR (2006). Differential expression of espin isoforms during epithelial morphogenesis, stereociliogenesis and postnatal maturation in the developing inner ear. Dev Biol 291, 83–95.
Siththanandan VB, Sellers JR (2011). Regulation of myosin 5a and myosin 7a. Biochem Soc Trans 39, 1136–1141.
Sorusch N, Bauss K, Plutniok J, Samanta A, Knapp B, Nagel-Wolfrum K, Wolfrum U (2017). Characterization of the ternary Usher syndrome SANS/ush2a/whirlin protein complex. Hum Mol Genet 26, 1157–1172.
Taylor R, Bullen A, Johnson SL, Grimm-Gunter EM, Rivero F, Marcotti W, Forge A, Daudet N (2015). Absence of plastin 1 causes abnormal maintenance of hair cell stereocilia and a moderate form of hearing loss in mice. Hum Mol Genet 24, 37–49.
Tokuo H, Mabuchi K, Ikebe M (2007). The motor activity of myosin-X promotes actin fiber convergence at the cell periphery to initiate filopodia formation. J Cell Biol 179, 229–238.
Umeki N, Jung HS, Watanabe S, Sakai T, Li XD, Ikebe R, Craig R, Ikebe M (2009). The tail binds to the head-neck domain, inhibiting ATPase activity of myosin VIIA. Proc Natl Acad Sci USA 106, 8483–8488.
Uyeda TQ, Abramson PD, Spudich JA (1996). The neck region of the myosin motor domain acts as a lever arm to generate movement. Proc Natl Acad Sci USA 93, 4459–4464.
Weck ML, Crawley SW, Stone CR, Tyska MJ (2016). Myosin-7b promotes distal tip localization of the intermicrovillar adhesion complex. Curr Biol 26, 2717–2728.
Weck ML, Grega-Larson NE, Tyska MJ (2017). MyTH4-FERM myosins in the assembly and maintenance of actin-based protrusions. Curr Opin Cell Biol 44, 68–78.
Weil D, Blanchard S, Kaplan J, Guilford P, Gibson F, Walsh J, Mburu P, Varela A, Levilliers J, Weston MD, *et al.* (1995). Defective myosin VIIA gene responsible for Usher syndrome type 1B. Nature 374, 60–61.
Weil D, Levy G, Sahly I, Levi-Acobas F, Blanchard S, El-Amraoui A, Crozet F, Philippe H, Abitbol M, Petit C (1996). Human myosin VIIA responsible for the Usher 1B syndrome: a predicted membrane-associated motor protein expressed in developing sensory epithelia. Proc Natl Acad Sci USA 93, 3232–3237.
Yang S, Huang FK, Huang J, Chen S, Jakoncic J, Leo-Macias A, Diaz-Avalos R, Chen L, Zhang JJ, Huang XY (2013). Molecular mechanism of fascin function in filopodial formation. J Biol Chem 288, 274–284.
Yang Y, Baboolal TG, Siththanandan V, Chen M, Walker ML, Knight PJ, Peckham M, Sellers JR (2009). A FERM domain autoregulates Drosophila myosin 7a activity. Proc Natl Acad Sci USA 106, 4189–4194.
Yang Y, Kovacs M, Sakamoto T, Zhang F, Kiehart DP, Sellers JR (2006). Dimerized Drosophila myosin VIIa: a processive motor. Proc Natl Acad Sci USA 103, 5746–5751.